iScience

CellPress
OPEN ACCESS

Article

COF-supported zirconium oxyhydroxide as a versatile heterogeneous catalyst for Knoevenagel condensation and nerve agent hydrolysis

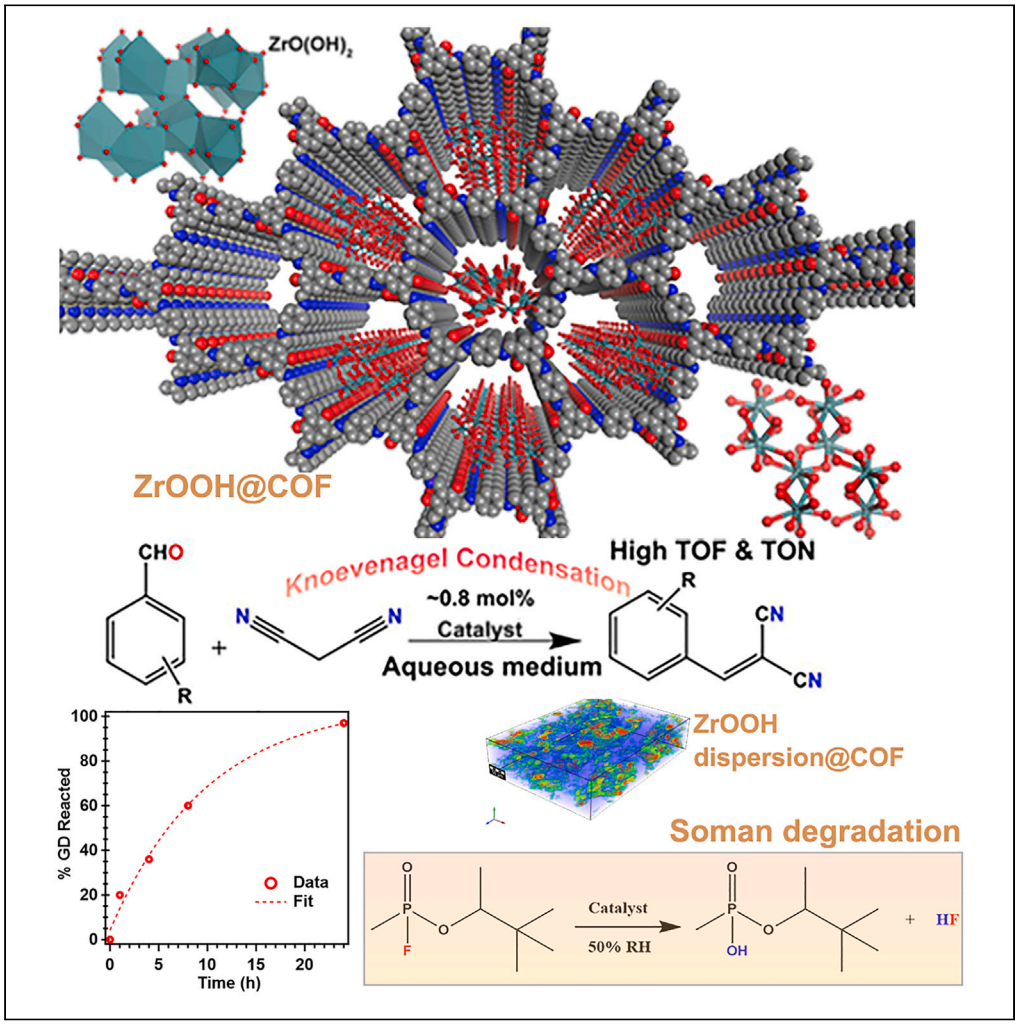

Pragalbh Shekhar, Venkata Swaroopa Datta Devulapalli, Reshma Reji, ..., Gregory W. Peterson, Eric Borguet, Ramanathan Vaidhyanathan

eborguet@temple.edu (E.B.)
vaidhya@acads.iiserpune.ac.in (R.V.)

Highlights

A facile synthesis of a hybrid of zirconium oxyhydroxides and COF, $ZrO_x(OH)_y$@COF

Improved catalytic properties of $ZrO_x(OH)_y$ by dispersing it on a COF

Catalyzes Knoevenagel condensation with high yields in water—a green catalyst

Hydrolyzes the nerve agent Soman with excellent kinetics—97% removal in 24 h

Shekhar et al., iScience 26, 108088
November 17, 2023
https://doi.org/10.1016/j.isci.2023.108088

iScience

CellPress
OPEN ACCESS

Article

COF-supported zirconium oxyhydroxide as a versatile heterogeneous catalyst for Knoevenagel condensation and nerve agent hydrolysis

Pragalbh Shekhar,[1,2,7] Venkata Swaroopa Datta Devulapalli,[3,7] Reshma Reji,[1,2,7] Himan Dev Singh,[1,2] Aleena Jose,[1,2] Piyush Singh,[1,2] Arun Torris,[4] Chatakudath P. Vinod,[5] John A. Tokarz III,[6] John J. Mahle,[6] Gregory W. Peterson,[6] Eric Borguet,[3,*] and Ramanathan Vaidhyanathan[1,2,8,*]

SUMMARY

A composite of catalytic Lewis acidic zirconium oxyhydroxides (8 wt %) and a covalent organic framework (COF) was synthesized. X-ray diffraction and infrared (IR) spectroscopy reveal that COF's structure is preserved after loading with zirconium oxyhydroxides. Electron microscopy confirms a homogeneous distribution of nano- to sub-micron-sized zirconium clusters in the COF. 3D X-ray tomography captures the micron-sized channels connecting the well-dispersed zirconium clusters on the COF. The crystalline $ZrO_x(OH)_y$@COF's nanostructure was model-optimized via simulated annealing methods. Using 0.8 mol % of the catalyst yielded a turnover number of 100–120 and a turnover frequency of 160–360 h^{-1} for Knoevenagel condensation in aqueous medium. Additionally, 2.2 mol % of catalyst catalyzes the hydrolysis of dimethyl nitrophenyl phosphate, a simulant of nerve agent Soman, with a conversion rate of 37% in 180 min. The hydrolytic detoxification of the live agent Soman is also achieved. Our study unveils COF-stabilized $ZrO_x(OH)_y$ as a new class of zirconium-based Lewis + Bronsted-acid catalysts.

INTRODUCTION

Covalent organic frameworks (COFs), a subclass of porous organic materials, are crystalline materials made of multifunctional organic building units connected by robust covalent bonds, resulting in stable structures with high surface areas and tunable porosities.[1–3] In addition to covalent bonding, ubiquitous hydrogen bonding and π-stacking interactions in COFs result in robust 2D/3D structures and protect them from hydrolysis and solvation.[4,5] Due to a diversity in the composition, structure, and properties, COFs are employed in a myriad of applications such as electrocatalysis,[6] charge storage,[7] dye degradation,[8] water remediation,[9–11] gas sorption,[12] storage and separation,[13] deposition/stabilization of metal nanoparticles (NPs),[8] and heterogeneous catalysis.[1,8,14]

Due to their elevated surface area-to-volume ratio, ultrafine metallic NPs are of special relevance for applications in heterogeneous catalysis.[1,15–18] However, due to the increased surface energy, NPs readily combine with smaller particles forming larger aggregates with diminished properties.[19] COFs exhibiting well-isolated pore channels help minimize the aggregation of deposited NPs and achieve control over the size of NPs.[20] Periodic layers of COFs connected by a distinctive channel structure allow for efficient access to active sites and rapid mass transport during catalysis.[21] Additionally, heteroatoms and surface functional groups in the COF pores can help in anchoring and stabilization of NPs, further preventing their aggregation.

Metal oxyhydroxides are metastable intermediates between metal hydroxides and metal oxides.[22] Though termed metastable, some metal oxyhydroxides exist in their crystallographic forms[23–25] up to 250°C–300°C and tend to decompose into metal oxides at higher temperatures.[26] A well-solved structure is not available for most metal oxyhydroxides. Although single crystal X-ray structure of $La_{0.26}Bi_{0.74}OOH$ is reported,[27] most other oxyhydroxides structures have been solved from powder X-ray diffraction (PXRD) using Rietveld methods.[23,28] However, to the best of our knowledge, the crystal structure of $ZrO_x(OH)_y$ is not known and it forms as an amorphous material, which at higher temperatures oxidizes to ZrO_2.[26]

[1]Department of Chemistry, Indian Institute of Science Education and Research, Pune 411008, India
[2]Centre for Energy Science, Indian Institute of Science Education and Research, Pune 411008, India
[3]Department of Chemistry, Temple University, Philadelphia, PA 19122, USA
[4]CSIR-NCL, Polymer Science and Engineering (PSE), Pune 411008, India
[5]CSIR-NCL Catalysis and Inorganic Chemistry Division, Pune, India
[6]U.S. Army DEVCOM Chemical Biological Center, Aberdeen Proving Ground, MD 21010, USA
[7]These authors contributed equally
[8]Lead contact
*Correspondence: eborguet@temple.edu (E.B.), vaidhya@acads.iiserpune.ac.in (R.V.)
https://doi.org/10.1016/j.isci.2023.108088

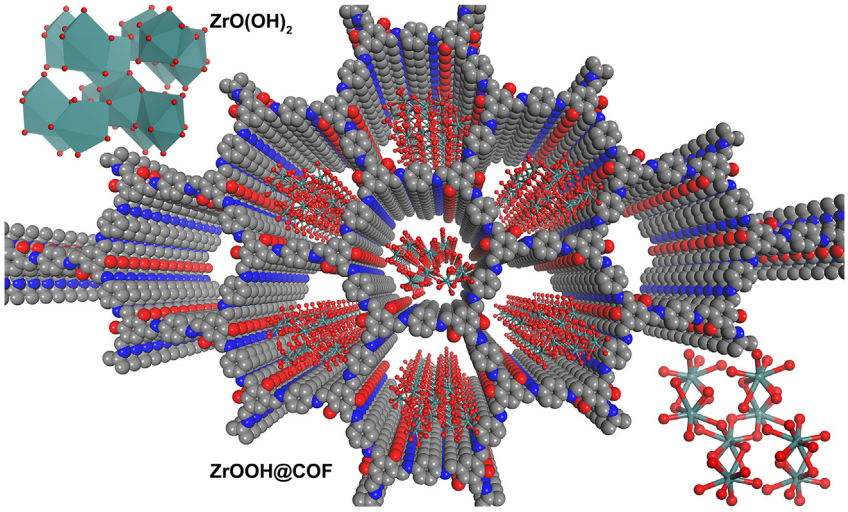

Figure 1. Structure of $ZrO(OH)_2$ and $ZrO_x(OH)_y$@COF

A DFT-optimized structure of $ZrO_x(OH)_y$@COF showing the 10 × 10 × 10 nanocluster of $ZrO_x(OH)_y$ derived from monoclinic $ZrO(OH)_2$ lattice[36] residing in the nanopores of the COF. Inset: Polyhedral (top left) and ball-and-stick (bottom right) model of the $ZrO(OH)_2$ cluster.

Metal oxyhydroxides have surface hydroxyl groups and M-*O*-M linkages, similar to those in metal hydroxides and metal oxides, respectively,[27] thus exhibiting attractive features of both classes of materials. Recent reports showed that zirconium oxyhydroxide, formed due to the hydrolysis of zirconium chloride, can actively degrade dimethyl nitrophenyl phosphate (DMNP),[29] a mimetic of the nerve agent Soman.[30] Surprisingly, the reported activity of zirconium oxyhydroxide was comparable to that of zirconium metal organic frameworks (MOFs) used for DMNP hydrolysis which contain similar zirconium clusters linked via biphenyl dicarboxylic acid linkers in a 3D fashion.[31–34] The instability of UiO-67 in water (releasing catalytic centers into solution) results in rapid hydrolysis of DMNP but limits the use of UiO-67 as a stable heterogeneous catalyst under aqueous conditions.[35]

To address this issue, we have synthesized zirconium oxyhydroxides clusters and deposited them on the imine-based IISERP-COF15. IISERP-COF15, made of readily available monomers, is chosen as a substrate as it has a high density of heteroatoms (N, O) which assist in anchoring the zirconium oxyhydroxide on the COF. The composite catalyst is characterized, and its catalytic properties for Knoevenagel condensation, DMNP hydrolysis, and Soman degradation are evaluated.

RESULTS AND DISCUSSION

Synthesis and characterization of $ZrO_x(OH)_y$@COF

$ZrO_x(OH)_y$@COF was prepared via a two-step process. Firstly, $ZrOCl_2.8H_2O$ was loaded into the COF using a double solvent method involving hexane and methanol (see method details, STAR Methods). $ZrOCl_2$@COF was dispersed in 50 mL of double distilled water and was stirred for 30 min. To this dispersion, 0.1 M NaOH solution was added drop by drop until the pH became 10–11; this yielded $ZrO_x(OH)_y$@COF. Detailed syntheses of materials can be found in the experimental section of the manuscript. The characterization (e.g., microscopy, porosity, and X-ray photoelectron spectroscopy) of neat COF, $ZrO_x(OH)_y$, and $ZrO_x(OH)_y$@COF is discussed in the supporting information (Figures S1–S18).

In order to better understand the structure of $ZrO_x(OH)_y$@COF, we constructed a 3D model of the $ZrO_x(OH)_y$@COF. A 10 × 10 × 10 nanocluster of the $ZrO_x(OH)_y$ was built from the monoclinic $ZrO(OH)_2$ lattice,[36] with every Zr center adopting capped pentagonal bipyramidal coordination geometry. Later, the nanocluster was dispersed within the COF lattice using grand canonical Monte Carlo (GCMC) methods. The final structure was optimized using the density functional theory (DFT) methods embedded in the CASTEP routine of the Materials Studio v.8.0. The optimized structure showed that each nanocluster was built from 8 zirconium centers, bridging and free hydroxyl as well as oxo centers, largely resembling the experimentally determined crystalline structure of $ZrO(OH)_2$.[36] Each cluster spans about the thickness of three COF layers, and their lateral dimensions fit well within the nanopores of the COF, as evident in the representative structure showing the pores of the COF filled with the oxyhydroxide clusters (Figure 1).

The crystalline nature of the synthesized COF was confirmed by PXRD. The characteristic low-angle, high intensity peak at $2\theta = 4.6^{o}$ and a few higher-angle peaks (Figure S1) support the successful formation of the COF.[37] PXRD of $ZrOCl_2.8H_2O$@COF displayed peaks from the COF, which are broader compared to that of COF suggesting a partial loss in crystallinity. No peaks were observed corresponding to $ZrOCl_2$ which implies either the absence of $ZrOCl_2$ or that the $ZrOCl_2$ is non-crystalline.

In the analysis of the PXRD patterns of the neat $ZrO_x(OH)_y$, we observe a broad peak at $2\theta = 31^{o}$ while the other peaks are of almost negligible intensity. This observation indicates the amorphous nature of $ZrO_x(OH)_y$, which is in good agreement with the reported literature[18] The deposition of $ZrO_x(OH)_y$ in COF leads to a partial loss in the crystallinity of the COF. However, the overall stability of the composite can be

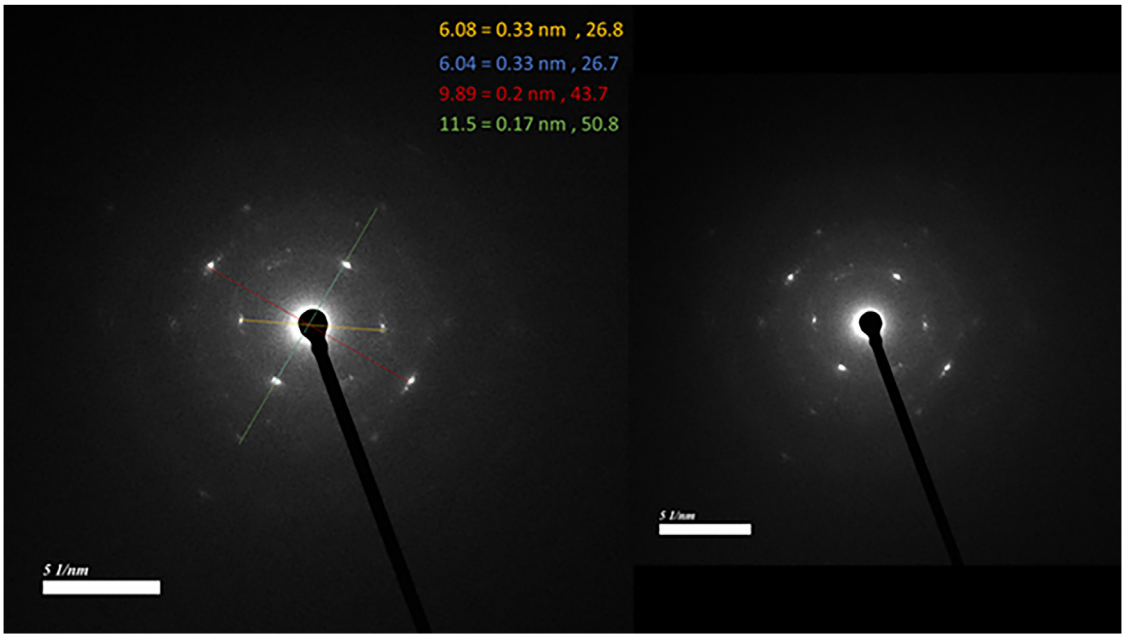

Figure 2. Crystallinity from TEM

SAED of $ZrO_x(OH)_y$@COF along the *[001]* direction looking at the hexagonal arrangement of zirconium centers 2θ = 26.8 => *(0 2 1) (1 2 0)*; 2θ = 43.5 => *(2 3 -1)*; 2θ = 50.8 => *(2 1 1)* (Please see the Figure S17 for the hexagonal arrangement in the direct crystallographic lattice).

confirmed by infrared (IR) spectroscopy of $ZrO_x(OH)_y$@COF, where in peaks at 1,517 cm^{-1} reveal the intact C=N functional groups on the COF and highlight the strong chemical bonding and robustness of the COF which helps survive the relatively harsh loading conditions (Figure S2).

Thermogravimetry of $ZrO_x(OH)_y$@COF under N_2 reveals that the sample is stable up to 400°C with an initial mass loss at 100°C corresponding to the loss of water molecules. A mass loss of about 60% at 400°C is observed, which corresponds to the decomposition of the COF (Figure S3). No significant mass loss is observed after 450°C, leaving behind thermally stable ZrO_2. Additionally, pyrolysis of $ZrO_x(OH)_y$@COF was performed at 600°C, and the PXRD pattern of the resulting material matched well with that of ZrO_2 reported in the literature (Figure S3).[18] This reveals that the metastable zirconium oxyhydroxide in COF is converted to stable zirconium oxide at temperatures above 450°C.[18]

The permanent porosity of neat COF was found by performing N_2 adsorption at 77 K. The COF shows a type-I isotherm with saturation N_2 uptake around 15 mmol g^{-1} and a Brunauer-Emmett-Teller (BET) and Langmuir surface areas of 1,286 and 1,449 m^2/g, respectively. However, the N_2 adsorption isotherm of $ZrO_x(OH)_y$@COF shows a reduced saturation N_2 uptake of 6 mmol g^{-1} compared to neat COF (15 mmol g^{-1}), indicating a lowering of available surface area due to the presence of oxyhydroxide particles in COF (Figures S4–S6).

Field emission scanning electron microscopy (FESEM) revealed a clumpier texture of IISERP-COF15, $ZrO_x(OH)_y$@COF, compared to $ZrOCl_2.8H_2O$@COF. However, the individual flakes of $ZrO_x(OH)_y$ and $ZrOCl_2$ were similar in size in $ZrO_x(OH)_y$@COF and $ZrOCl_2.8H_2O$@COF respectively (Figures S8–S11). Energy dispersive X-ray analysis (EDAX) analysis of $ZrOCl_2.8H_2O$@COF and $ZrO_x(OH)_y$@COF suggested 10% and 8 wt % of zirconium loading, respectively, which were further verified by inductively coupled plasma (ICP) analysis (10.4% and 8.2% zirconium loading, respectively) (Figures S12 and S13), and the elemental mapping shows a homogeneous distribution of zirconium over the COF (Figure S14), supporting our observations made using 3D tomography.

High-resolution transmission electron microscopy (HRTEM) was performed on the neat COF and $ZrO_x(OH)_y$@COF to study the local structure and microscopic crystallinity. The images confirm the formation of the COF as large micron-sized flakes and reveal the presence of uniform micropores in the COF. Polycrystalline rings were observed in the selected area electron diffraction (SAED) pattern, and lattice fringes could also be seen. It is indexed to the *(00l)* reflection corresponding to the COF's interlayer spacing (d = 0.33 nm) (Figure S15). Meanwhile, for the $ZrO_x(OH)_y$@COF, all these features were seen, and in addition, relatively strong diffraction spots from the inorganic component, $ZrO_x(OH)_y$, were observed. These were indexed to the reflection planes *(0 2 1)*, *(1 2 0)*, *(2 3 -1)*, and *(2 1 1)*, which represent the strong diffraction peaks observed for the bulk phase of $ZrO(OH)_2$ crystallized in the P2/m setting.[36] The hexagonal arrangement of the strongest spots indexed to the *(0 2 1)* plane can be assigned to the arrangement of the zirconium atoms along the *[00l]* direction. Notably, this corresponds to a 2θ = 26.8º, which overlaps with the *(0 0 l)* reflection of the COF- the π-stacking direction (Figures 2, S16, and S17). Thus, confining the $ZrO_x(OH)_y$ clusters within the COF exposes selected facets of the lattice, which most likely are the active facets involved in the catalysis.

Identifying the oxidation states of zirconium and other elements is essential to understand the coordination environment of potential catalytic sites in $ZrO_x(OH)_y$@COF. To this end, we performed X-ray photoelectron spectroscopy (XPS). The deconvolution of Zr3d spectrum shows peaks at 181.78 eV, 184.14 eV, 182.24 eV, and 184.6 eV, corresponding to ZrO_2 ($3d_{5/2}$ and $3d_{3/2}$) and Zr-OH ($3d_{5/2}$ and $3d_{3/2}$) with peak separation of 2.36 eV, respectively (Figure 3).[38] These match the peaks observed for $ZrO_x(OH)_y$ NPs (Figure S18).[38] In addition, for

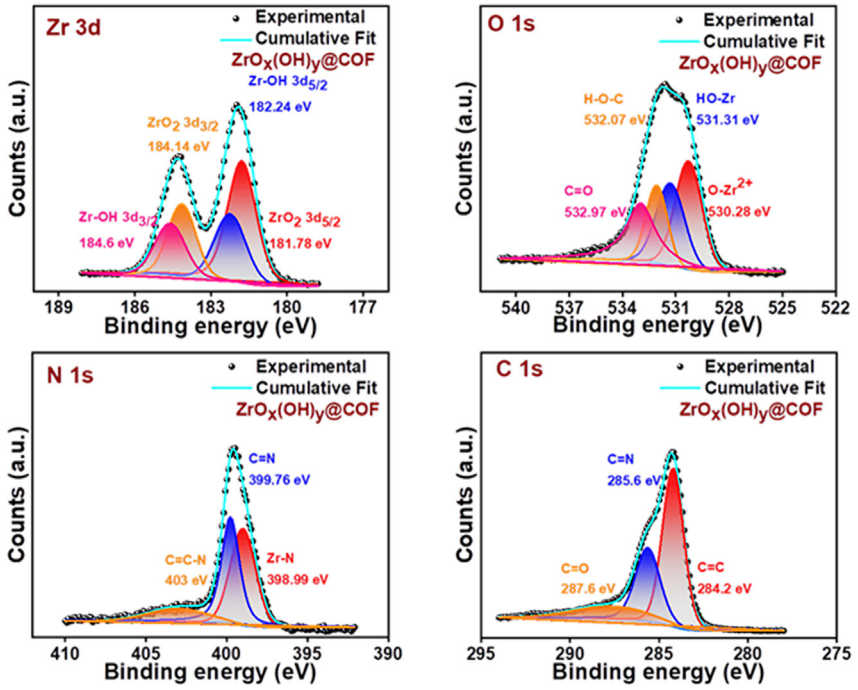

Figure 3. Composition of $ZrO_x(OH)_y$@COF

XPS spectra of $ZrO_x(OH)_y$@COF showing the presence of oxide and hydroxide coordination to zirconium centers.

O1s spectrum, peaks were observed at 530.28 eV (O-Zr), 531.31 eV (HO-Zr), 532.07 eV (H-O-C), and 532.97 eV (C=O) which suggest the binding modes of oxygen with Zr[39] and those in the COF. The deconvolution of N 1s spectrum displays peaks at 398.99 eV, 399.76 eV, and 403 eV, which denote Zr-N, C=N, and C=C-N interactions, respectively.[37] These results suggest the presence of Zr-O and Zr-OH which further confirms that the synthesized material is the metastable $ZrO_x(OH)_y$ which is strongly interacting with the nitrogen atoms of the COF.

Micron-level structure of the supported catalyst from 3D tomography

To shed light on the microstructure of the $ZrO_x(OH)_y$@COF, we resorted to 3D tomography imaging, which reveals that the oxyhydroxide clusters form as large islands which are dispersed in the COF framework (Figure 4). Although 3D tomography suggests a higher zirconium loading of ~14 wt %, the sample area under consideration was only from a micron resolution. In contrast, the ~8 wt % determined by EDAX and ICP analysis is more quantitative since the entire sample is considered (Figure S13). Importantly, these 3D images convey two prominent features: (i) in the majority, the $ZrO_x(OH)_y$ do not form as isolated discrete clusters nano-confined in the COF pores and (ii) the $ZrO_x(OH)_y$ structures are well-dispersed even at the micron level, and there is sufficient microporosity in the overall catalyst, which connects these catalytically active inorganic centers.

Knoevenagel condensation using $ZrO_x(OH)_y$@COF

The Knoevenagel condensation reaction (Scheme 1) is an important organic transformation allowing construction of C-C bonds, using aldehyde/ketone and active methylene group containing molecules that undergo nucleophilic addition to the carbonyl compound followed by the removal of a water molecule to yield the desired product.[40] Malononitrile is one of the most commonly employed active methylene compounds for Knoevenagel reaction due to its availability and ease of handling.[41] Knoevenagel condensation has been reported with different heterogeneous catalysts such as nitrided ITQ-2,[42] nickel iron hydrotalcite,[43] Cu_3TATAT,[44] MIL-100(Fe),[45] Cr-MIL-101-NH_2,[46] Ru/Zr-UiO-66,[47] and CAU-1-NH_2.[48] However, the limitations of these works include difficulty in catalyst synthesis, poor stability of the catalyst, elevated reaction conditions (e.g., 60°C–100°C), and the use of non-aqueous solvents.[49–51] Earlier, we and others had reported the use of COF in synthesizing catalytically active metal compounds in NP in a capping agent-free method.[52] In those materials, typically, the Co-, Ni-, and Pd-based compounds were employed. Here, we are interested in stabilizing a rapidly emerging Lewis acidic higher oxidation state zirconium oxyhydroxide compound. To the best of our knowledge, there are no reports on employing COF-supported $ZrO_x(OH)_y$ as a catalyst for Knoevenagel condensation.

Knoevenagel condensations can be accelerated by a Brønsted base where the basic sites abstract protons from malononitrile molecules to form a carbanion intermediate.[53] Acid-base bifunctional catalysts can activate electrophiles and nucleophiles simultaneously and can hence effectively catalyze Knoevenagel condensation. Deriving the structural aspects from the lanthanum oxyhydroxides[23] and the Zr-oxy-hydroxo clusters proposed in solution,[54] the amorphous bulk zirconium oxyhydroxide powder can be expected to have a large number of surface

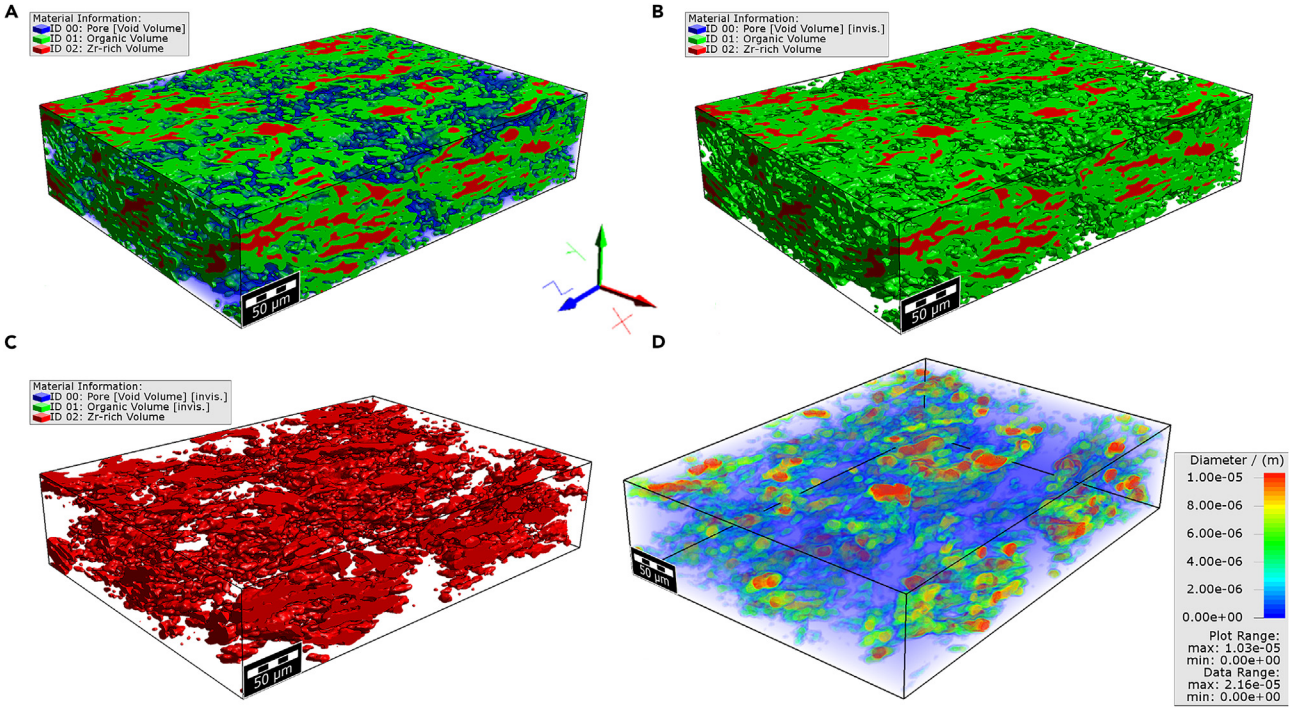

Figure 4. Distribution of the zirconium cluster in the COF

Three-dimensional X-ray tomography images displaying the distribution of zirconium cluster (red), organic COF (green), and pores (blue) within $ZrO_x(OH)_y$@COF.

(A) All three are represented: Volume %: Void Volume = 49.5 (Porosity); Organic volume = 36.0; Zr-rich volume = 14.5.

(B) Dispersion of the inorganics in the COF.

(C) Zirconium cluster distribution. Note the presence of large islands suggesting a multi-zirconium cluster from extended $ZrO(OH)_2$ lattice.

(D) Displays the particle size distribution within the composite.

hydroxyl groups that are acidic and deprotonate in the presence of water to give Brønsted basic sites. It is also anticipated that Zr-*O*-Zr linkages can provide basicity in the form of Lewis basic O^{2-} and Lewis acidic zirconium. Therefore, $ZrO_x(OH)_y$@COF is expected to be a potential acid-base bifunctional catalyst and efficiently catalyze Knoevenagel condensation reactions. Meanwhile, the COF could provide the required nanoconfinement by acting as a molecular container for hosting the substrates and the $ZrO_x(OH)_y$. The plausible mechanism is shown in Figure S19.

In order to identify suitable solvents for high yields of products of Knoevenagel condensation, we screened the widely used media such as acetonitrile, ethanol, etc. Surprisingly, using $ZrO_x(OH)_y$@COF as catalyst, we observed a higher yield of products in water compared to ethanol and acetonitrile (Table S1). Moreover, the condensation reaction proceeds to completion at room temperature as opposed to elevated conditions[41] in a short span of 30 min. The superiority of the reaction metrics can be attributed to the fact that the active oxyhydroxides are homogeneously dispersed in the COF matrix and do not aggregate as they might in water, allowing for easy diffusion of reactants toward the catalytic centers. The high yield in water can be attributed to its high dielectric constant and cohesive energy density that are reported to favor reaction kinetics and yields.[55] This result suggests that we can perform a "green" Knoevenagel condensation using $ZrO_x(OH)_y$@COF.

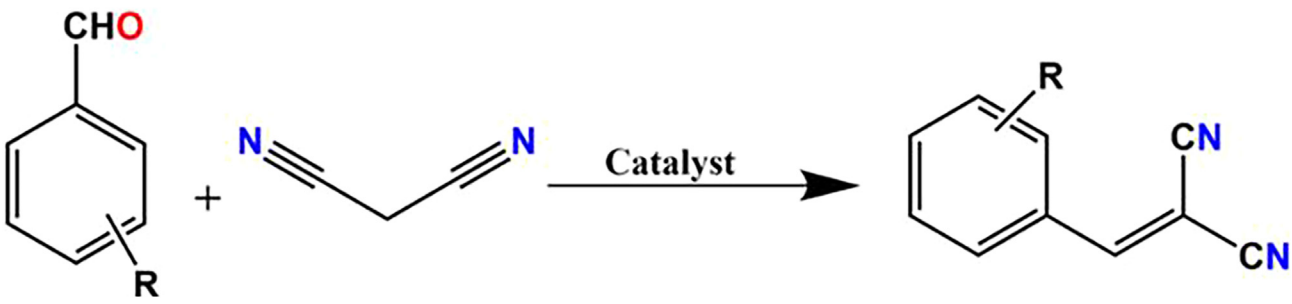

Scheme 1. Reaction scheme of Knoevenagel condensation using substituted benzaldehydes and malononitrile.

Table 1. Summary of the yield of Knoevenagel condensations performed using 1 mmol each of aldehyde and malononitrile in 5 ml solvent and 0.8 mol% $ZrO_x(OH)_y$@COF at specified temperature and time

S. no	Substrate	Product	Time (mins)	Yield (%)	TON	TOF (h^{-1})
1.	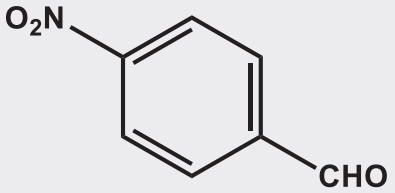	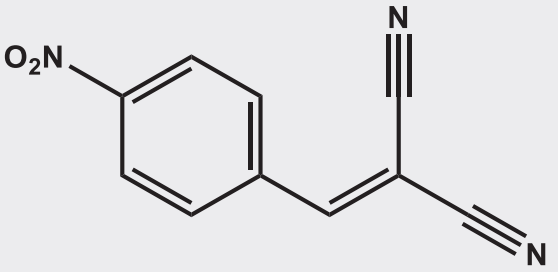	20	95	119	357
2.	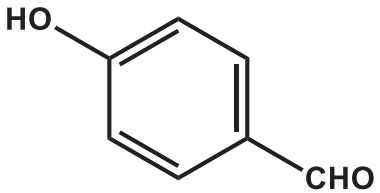	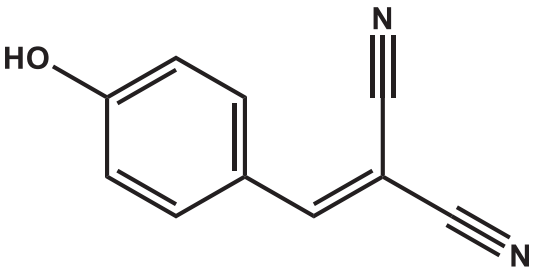	30	82	103	206
3.	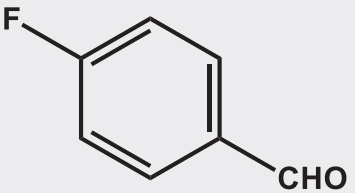	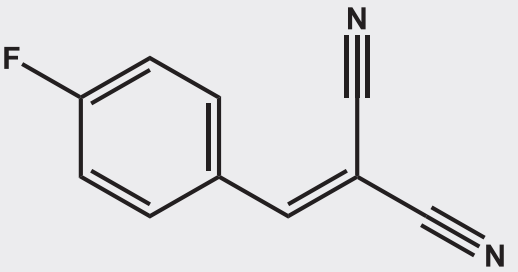	40	89	111	167
4.	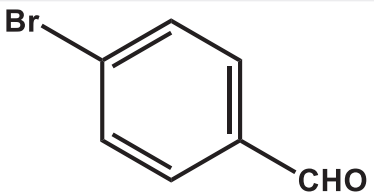	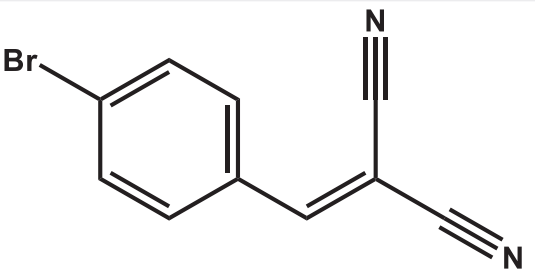	30	92	115	230

(*Continued on next page*)

Table 1. *Continued*

S. no	Substrate	Product	Time (mins)	Yield (%)	TON	TOF (h^{-1})
5.	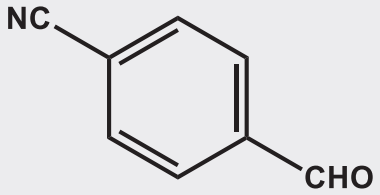	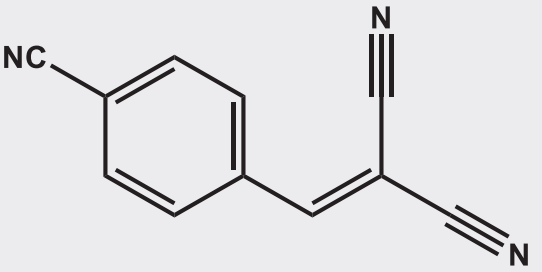	30	96	120	240
6.	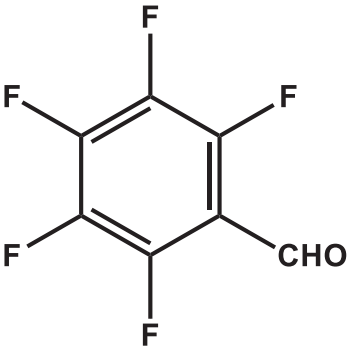	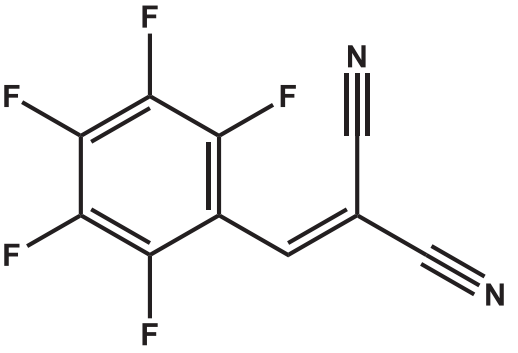	30	90	113	226
7.	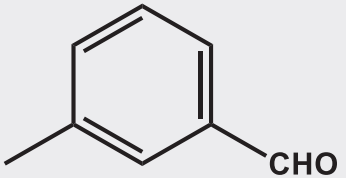	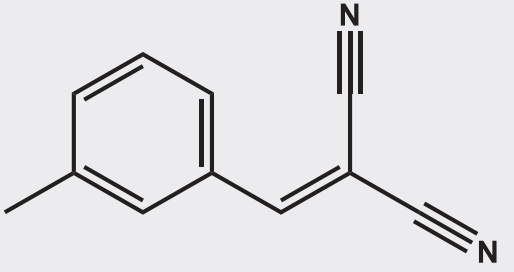	40	87	109	164

(*Continued on next page*)

Table 1. ***Continued***

S. no	Substrate	Product	Time (mins)	Yield (%)	TON	TOF (h^{-1})
8.	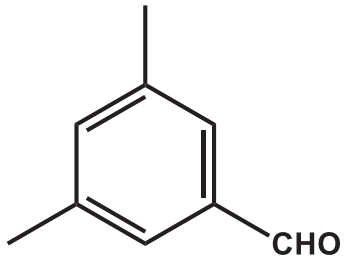	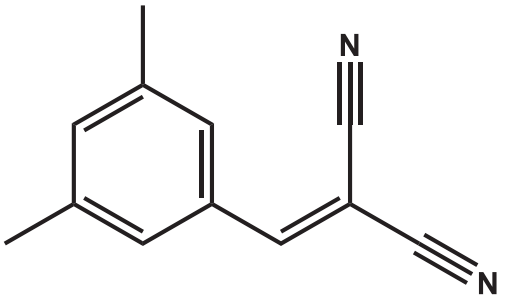	30	85	106	212
9.	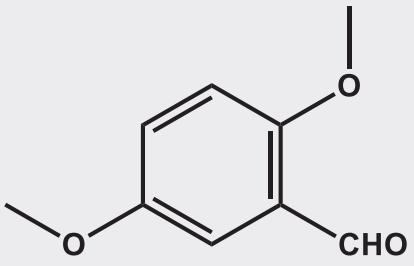	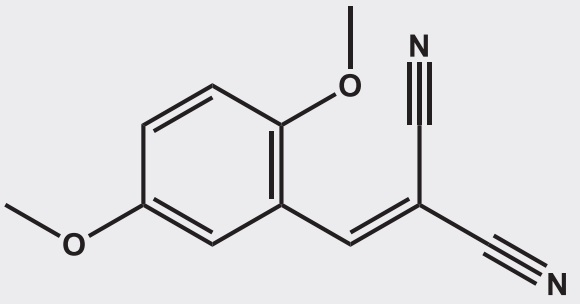	30	91	114	228
10.	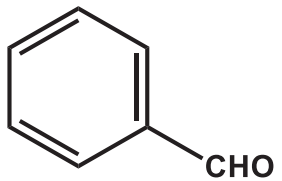	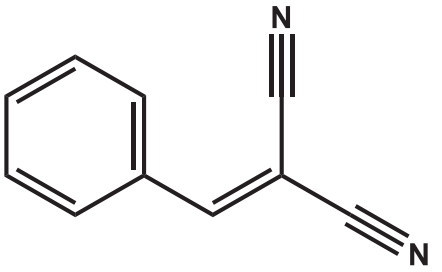	30	95	119	238

Note that the TON and TOF values are calculated by taking x and y as 1 and 2, respectively.

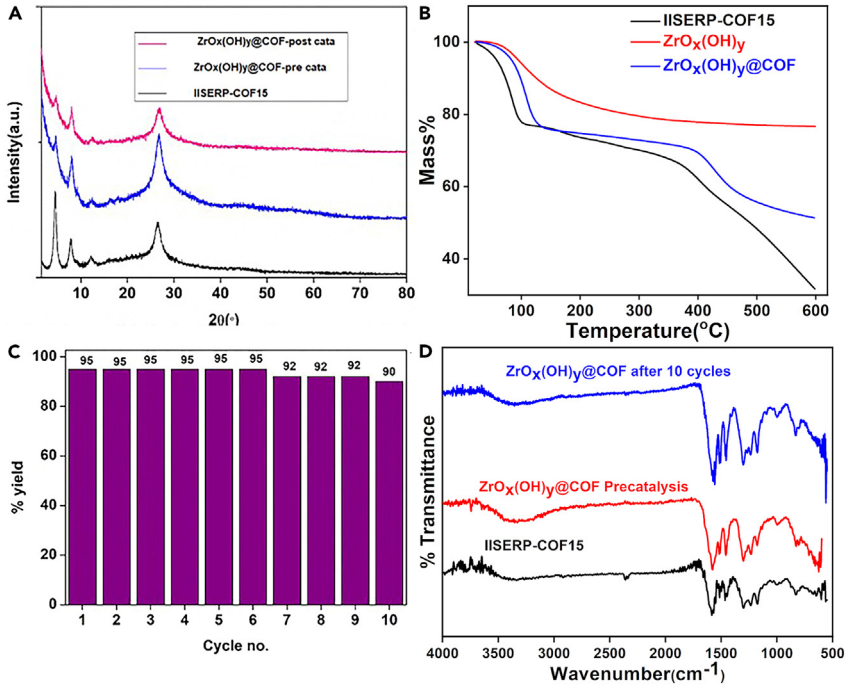

Figure 5. Recyclability and stability of $ZrO_x(OH)_y$@COF for Knoevenagel condensation—spent catalyst analysis

(A) PXRD of IISERP-COF15, $ZrO_x(OH)y$@COF and $ZrO(Cl)_2.8H_2O$@COF.

(B) TGA curves of IISERP-COF15, $ZrO_x(OH)_y$ and $ZrO_x(OH)_y$@COF.

(C) $ZrO_x(OH)_y$@COF recyclability over 10 cycles.

(D) IR spectra comparisons.

Our experiments reveal $ZrO_x(OH)_y$@COF to be an efficient heterogeneous catalyst for Knoevenagel condensation between benzaldehyde derivatives (substituted with electrophilic and nucleophilic groups) and malononitrile, performed in water. Carrying out these reactions in water is not only environmentally benign but also provides the best conditions to realize the maximum Brønsted acidity from these surface hydroxyls, given the catalyst presented here is stable to the humid environments. By employing 0.8 mol % of catalyst, significantly lower than the previously reported cases, we obtained a yield of 85%–95% for a wide variety of substrates (with electron-withdrawing/donating groups on the benzaldehyde substrate) with a high turnover number (TON) of ~ 100–120 and turnover frequency (TOF) ~160—360 h^{-1} as reported in Table 1. However, using $ZrO_x(OH)_y$ or $ZrOCl_2.8H_2O$ or without the catalyst the reactions do not proceed to completion. (Table S2).

In 2008, Vijender and coworkers used zirconium tetrachloride adsorbed on silica gel as a catalyst for the synthesis of substituted electrophilic alkenes by Knoevenagel condensation.[56] With 10 mol % of the catalyst, they obtained a yield of 85%–93% in 2–4 h by carrying out the reactions at 80°C–85°C in acetonitrile. The catalytic activity was found to be intact up to three cycles of reaction.[56] Malakooti et al. developed pure monoclinic zirconia NPs for catalyzing Knoevenagel condensation. With nearly 12 mol % of catalyst, they obtained a yield of 90%–95% in 2–3 h by carrying out the reaction at 78°C using ethanol as a solvent.[57] In 2021, Liu and coworkers employed bifunctional zinc MOF bearing triazole-carboxylate mixed ligand as a catalyst for Knoevenagel condensation reactions. With 5 mol % of catalyst, they obtained a yield of 17%–100% in 2 h at room temperature by using water as a solvent.[58] In 2020, Laha and coworkers used Co(II)-organic frameworks as a catalyst for Knoevenagel condensation reactions and obtained a yield of 60%–100% and TON of 30–50 with 2 mol % of catalyst in 1 h at room temperature using methanol as a solvent.[59] Meanwhile, Zuo et al.[60] employed amorphous Zr-porphyrin to catalyze Knoevenagel condensations. These reports employ either harsh temperatures or use non-aqueous solvents including ionic liquids and result in low yields. Table S3 provides a comparison of the reaction conditions, solvents employed, yields, and TOF values of reported catalysts to those of present work highlighting the advantages of using $ZrO_x(OH)_y$@COF. To the best of our knowledge, $ZrO_x(OH)_y$@COF has the highest TOF values (160-360 h^{-1}) while allowing optimum reaction conditions (temperature, solvent, etc) compared to reported zirconium- and COF-based materials.

Catalyst stability and recyclability for Knoevenagel condensation

In order to test the stability of $ZrO_x(OH)_y$@COF during the reaction, the catalyst was filtered from the reaction mixture and washed with water and methanol to remove any reactants or products. The catalyst dried at 80°C was subjected to successive cycles of Knoevenagel condensation. After each cycle of the reaction, filtration and washing were repeated and the catalyst was used for 10 cycles of reaction. We observed little to no loss in the catalytic activity of the catalyst after ten cycles (Figure 5) which is indicative of the robust nature of the catalyst. After completion of 10 cycles of reaction, the recovered catalyst was characterized using different techniques like PXRD, IR spectroscopy,

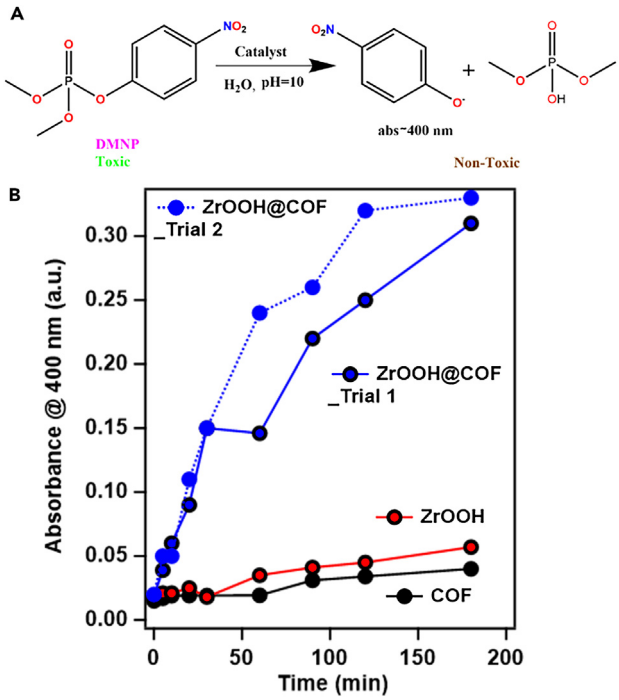

Figure 6. DMNP hydrolysis using $ZrO_x(OH)_y$@COF

(A) Hydrolysis scheme of DMNP.

(B) Absorbance at 400 nm vs. time graph showing the progress of DMNP hydrolysis using $ZrO_x(OH)_y$@COF, $ZrO_x(OH)_y$, and COF.

FESEM, EDAX studies, and elemental mapping (Figures 5, S20, and S21). The characteristic PXRD peaks of the loaded COF remain intact, showing that even after 10 cycles of reaction, the functional integrity of the loaded COF is preserved though there is a slight loss in crystallinity after 10 cycles. The characteristic IR peaks of the COF remain intact after 10 cycles of reaction. The FESEM images show that the morphology of loaded COF is preserved after 10 cycles. Elemental mapping of $ZrO_x(OH)_y$@COF after 10 cycles of catalysis still shows a homogeneous distribution of elements (Figures S20 and S21). The energy dispersive X-ray (EDX) analysis of $ZrO_x(OH)_y$@COF after catalysis shows the amount of zirconium to be ~7.6 wt % (Figure S21), which is further verified by ICP analysis (7.9% zirconium loading). Thus the characterization of the spent catalyst, after 10 cycles, highlights the stability and efficacy of $ZrO_x(OH)_y$@COF. The XPS spectra of the spent catalyst were recorded (Figure S22A). The peaks from C1s, O1s, N1s, and Zr3d levels were observed with expected binding energies. The C1s and N1s appeared very similar to the parent catalyst. However, there was a noticeable change in the O1s and Zr3d peak profiles. The former becomes relatively sharper, while the latter is weaker and broad. The broad signal for Zr3d is indicative of a non-stoichiometric O/Zr ratio;[61–63] or in other words the zirconium adopts mixed valence balanced by a mixture of O^{2-} and OH^- species in this system. This suggests the zirconium species is catalytically active. The signal is weaker because the catalyst is likely deeply buried in the COF, as in earlier cases.[64] To evaluate the spent catalyst's surface area, we resorted to BET measurements. The 77K N_2 adsorption isotherm of the spent catalyst showed the same type 1 behavior as the parent catalyst; however, the N_2 uptake had dropped, and the surface area had reduced from 524 to 265 m^2/g (Figure S22B). This also points to the potential burying of zirconium species into the COF matrix leading to a relatively denser catalyst. And this in-action catalyst's surface area is still a significant value.

Nerve agent and simulant hydrolysis using $ZrO_x(OH)_y$@COF

Previous studies have shown that secondary building units of MOF (M-O-M linkages) mimic the chemistry of the active site of phosphotriesterase enzyme and hence hydrolyze the P-X bond in nerve agents as well as their simulants.[65] Devulapalli et al.[29] reported that metal precursors of UiO-67 ($ZrCl_4$, $HfCl_4$, and $Zr(OH)_4$) also hydrolyze DMNP, almost as efficiently as the MOFs, and the activity of the MOF precursors was determined to be proportional to their Lewis acidity. The hexa-zirconium clusters embedded into a polymer also catalyzed the nerve agent degradation.[66]

In this work, employing only 2.2 mol % (Zr content ~0.21 mg) of $ZrO_x(OH)_y$@COF, which is an order of magnitude lower than the amount of zirconium (3 mg) reported by Devulapalli et al., results in significant DMNP hydrolysis (37%) after nearly 3 h. The catalytic activity of $ZrO_x(OH)_y$@COF was observed to be higher than the catalytic activity of neat $ZrO_x(OH)_y$ and as-made COF as indicated by the ultraviolet-visible (UV-vis) profile showing the progress of DMNP hydrolysis with time (Figure 6, Table S4). The higher activity of $ZrO_x(OH)_y$@COF over its precursors can be attributed to the dispersed reactive surface hydroxyl groups of $ZrO_x(OH)_y$ on the COF which facilitate easy access of the reactant molecules to catalytic sites, resulting in a TON and TOF of 1.54 and 0.5 h^{-1}, respectively. These observations reveal the true

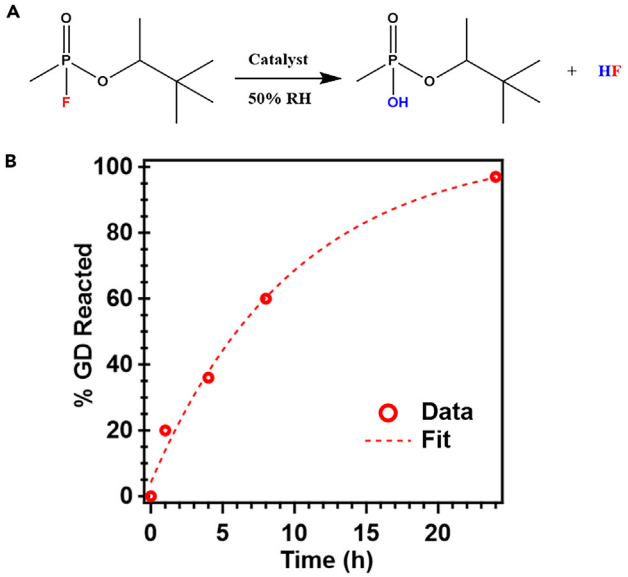

Figure 7. Soman degradation using $ZrO_x(OH)_y$@COF

(A) Hydrolysis scheme of Soman.

(B) Kinetics plot showing the degradation of Soman over time.

heterogeneous nature of $ZrO_x(OH)_y$@COF and its catalytic ability. Based on the reactivity toward DMNP, $ZrO_x(OH)_y$@COF was evaluated against the nerve agent Soman (GD) and exhibited 97% removal (liquid dosed on solid $ZrO_x(OH)_y$@COF) over a 24 h period (Figure 7; see method details, STAR Methods). These data showcase the ability of the material to decontaminate and detoxify highly toxic nerve agents.

Conclusion

In summary, we report the successful synthesis of heterogeneous $ZrO_x(OH)_y$@COF—a catalyst with accessible, reactive surface hydroxyl groups of oxyhydroxides deposited on an imine COF. Using the synthesis protocols employed, we achieve about 8% loading of zirconium which also resulted in a homogeneous distribution of zirconium, as confirmed by elemental mapping. $ZrO_x(OH)_y$@COF gave excellent yields for Knoevenagel condensation in substrates with both electron-donating and electron-withdrawing groups (0.8 mol % of catalyst exhibiting a TOF of 164–357 h^{-1} at room temperature in water). $ZrO_x(OH)_y$@COF showed high recyclability with little drop in yield of product for up to 10 consecutive cycles, which highlights the stability and applicability of the catalyst system. $ZrO_x(OH)_y$@COF can be classified as a green catalyst as the Knoevenagel condensation occurs in water, without the use of a base. $ZrO_x(OH)_y$@COF was found to catalytically hydrolyze DMNP with a 37% conversion in nearly 180 min showing a higher activity than as-made zirconium oxyhydroxide powder and COF. Our work underscores the importance of heterogenization and stabilization of active nanoporous catalysts on supports such as COFs, which can provide anchoring sites and pave the way for the development of superior oxyhydroxide systems (e.g., using other Lewis acidic metals such as hafnium, cerium) for catalyzing various organic/inorganic reactions.

Limitations of the study

The layered COF material described here generally forms as highly insoluble polycrystalline powders; hence, their experimental structure determination from single crystal X-ray diffraction or electron diffraction is very difficult. Therefore, we resort to crystallographic modeling.

The live test carried out using the nerve agent Soman is not accessible to all as the Soman is a restricted chemical. This makes our findings valuable.

STAR★METHODS

Detailed methods are provided in the online version of this paper and include the following:

- KEY RESOURCES TABLE
- RESOURCE AVAILABILITY
  - Lead contact
  - Materials availability
  - Data and code availability

APPENDIX

Nuclear Magnetic Resonance Spectroscopy (NMR) of products of Knoevenagel condensation (See Figures S24–S34 of the supporting information).

Computational details

We constructed a 3D model of the $ZrO_x(OH)_y$@COF utilizing Materials Studio Version 8.0 software. For this, we built a 10 × 10 × 10 nanocluster of the $ZrO_x(OH)_y$ from the monoclinic $ZrO(OH)_2$ lattice (Baklanova, Y. V.; Denisova, T. A.; Maksimova, L. G.; Tyutyunnik, A. P.; Baklanova, I. V.; Shein, I. R.; Neder, R. B.; Tarakina, N. V., Synthesis and characterization of new $MO(OH)_2$ (M = Zr, Hf) oxyhydroxides and related Li_2MO_3 salts. Dalton Transactions 2014, 43 (7), 2755–2763), with every Zr center adopting capped pentagonal bipyramidal coordination geometry. Later, the nanocluster was dispersed within the COF lattice using Grand Canonical Monte Carlo (GCMC) methods. We optimized the final structure using the DFT methods embedded in the CASTEP routine of the Materials Studio v.8.0. The structure had each nanocluster built from 8 Zr-centers, bridging and free hydroxyl as well as oxo centers, largely resembling the experimentally determined crystalline structure of $ZrO(OH)_2$. Each cluster spans about the thickness of three COF layers, and their lateral dimensions fit well within the nanopores of the COF. The final structure was geometry optimized using the Ab Initio Total Energy Program CASTEP embedded in the Accelrys program, which uses the DFT Semi-Empirical Dispersion interaction Correction module (First principles methods using CASTEP", Zeitschrift fuer Kristallographie, 220(5–6) pp. 567–570 (2005), S. J. Clark, M. D. Segall, C. J. Pickard, P. J. Hasnip, M. J. Probert, K. Refson, M. C. Payne; Erik R. McNellis, Joerg Meyer, and Karsten Reuter, Phys. Rev. B 80, 205414 (2009)).

GCMC parameters for the dispersion of $ZrO(OH)_2$ nanoclusters into the COF: 1000000 equilibration steps were calculated using the Metropolis algorithm employing a Universal forcefield. The Lennard–Jones equation, with a cut-off radius of 12.5 Å, was used to calculate the van der Waals interactions. The long-range electrostatic and Coulomb interactions were obtained by three-dimensional Ewald Group methods, with an accuracy of 1.0e-5 kcal/mol.

CASTEP optimization parameters for the $ZrO_x(OH)_y$@COF: LJ dispersions were used to determine van der Waals interactions, and self-consistent charges were used to determine the Coulombic interaction between partial atomic charges. Considering the periodic structure and the hybrid nature of the system (inorganic-organic), the exchange correlations were handled using the generalized gradient approximations (GGAs); self-consistent charges were used to determine the Coulombic interaction between partial atomic charges. We included UFF-based Lennard-Jones dispersion corrections in Energy, Force and Displacement calculations. All calculations are at 0K and were spin-unrestricted, adopting the formal spin as the initial spin. A plane wave basis set cut-off was kept as 381 eV. For our dispersion-corrected DFT, we used Generalized Gradient Approximation (GGA) to calculate the exchange and the correlation energies that employ the Perdew-Wang 91 (PW91) exchange potential. Pulay density mixing schemes were used. The total energy/Eigen energy tolerance was kept high at a value of 0.5 x 10-5 eV. OTFG Ultrasoft potentials were employed for the BFGS geometry optimization. (Pfrommer, B. G.; Cote, M.; Louie S. G.; Cohen, M. L. "Relaxation of Crystals with the Quasi-Newton Method," J. Comput. Phys., 131, 233–240 (1997)). The structure converged well with acceptable bond distances and angles to a total energy of −81957 eV in the ground state at 0K. No restrictions were applied during the optimization.

SUPPLEMENTAL INFORMATION

Supplemental information can be found online at https://doi.org/10.1016/j.isci.2023.108088.

ACKNOWLEDGMENTS

This project received support from the Defense Threat Reduction Agency (DTRA), United States, Grant no. HDTRA1-21-1-0019, and the Air Force Office of Scientific Research, United States, under Award Number FA2386-21-1-4022. The authors thank DST for material for energy storage (DST/TMD/MES/2k17/103) program and the "DST-Nanomission under the Thematic Unit Program" (EMR/2016/003553), India. We acknowledge the Science and Engineering Research Board (SERB) (CRG/2021/008250), India. We acknowledge National Supercomputing Mission (NSM) for providing computing resources of 'PARAM Brahma' at IISER Pune, which is implemented by C-DAC and supported by the Ministry of Electronics and Information technology (MeitY) and Department of Science and Technology (DST), Government of India. The authors thank the Defense Threat Reduction Agency Joint Science and Technology Office, United States, for Chemical Biological Defense for funding and Jim Buchanan for supporting GD testing.

AUTHOR CONTRIBUTIONS

P.S., V.S.D.D., and R.R.: Contributed equally; V.S.D.D.: Conceived the concept; P.S., V.S.D.D., and R.R.: Designed and performed catalysis experiments, manuscript writing and proof reading, and intellectual contributions; P.S and H.D.S contributed equally to designing and performing the characterization experiments on the materials, data analysis and plotting, manuscript writing, and proof reading; A.J.: Synthesized the COF and the catalyst in multiple batches and characterized them. P.S.: Measured the spent catalyst adsorption isotherms, calculated the BET surface area, and analyzed the spent catalyst XPS data. A.T.: Carried out the X-ray tomography experiment and analysis; C.P.V.: Performed the XPS measurements and helped with the data analysis and interpretation; J.A.T.: conducted GD testing; G.W.P.: analyzed GD data, developed kinetic equations, provided input to the manuscript; J.J.M.: provided input into GD testing and provided feedback to the manuscript. All authors have given approval to the final version of the manuscript; R.V. and E.B.: Conceived the concept, designed experiments, contributed to manuscript writing and proof reading, and made intellectual contributions.

DECLARATION OF INTERESTS

The authors declare no competing interests.

Received: May 31, 2023
Revised: June 25, 2023
Accepted: September 26, 2023
Published: September 30, 2023

REFERENCES

1. Mullangi, D., Nandi, S., Shalini, S., Sreedhala, S., Vinod, C.P., and Vaidhyanathan, R. (2015). Pd loaded amphiphilic COF as catalyst for multi-fold Heck reactions, C-C couplings and CO oxidation. Sci. Rep. *5*, 10876–10912.
2. Haldar, S., Kushwaha, R., Maity, R., and Vaidhyanathan, R. (2019). Pyridine-Rich Covalent Organic Frameworks as High-Performance Solid-State Supercapacitors. ACS Mater. Lett. *1*, 490–497.
3. Mullangi, D., Shalini, S., Nandi, S., Choksi, B., and Vaidhyanathan, R. (2017). Super-hydrophobic covalent organic frameworks for chemical resistant coatings and hydrophobic paper and textile composites. J. Mater. Chem. A *5*, 8376–8384.
4. Abuzeid, H.R., EL-Mahdy, A.F., and Kuo, S.W. (2021). Covalent organic frameworks: Design principles, synthetic strategies, and diverse applications. Giant *6*, 100054.
5. Ma, D., Wang, Y., Liu, A., Li, S., Lu, C., and Chen, C. (2018). Covalent Organic Frameworks: Promising Materials as Heterogeneous Catalysts for C-C Bond Formations. Catalysts *8*, 404.
6. Tang, J., Su, C., and Shao, Z. (2021). Covalent Organic Framework (COF)-Based Hybrids for Electrocatalysis: Recent Advances and Perspectives. Small Methods *5*, e2100945.
7. Zhao, H., Chen, H., Xu, C., Li, Z., Ding, B., Dou, H., and Zhang, X. (2021). Charge Storage Mechanism of an Anthraquinone-Derived Porous Covalent Organic Framework with Multiredox Sites as Anode Material for Lithium-Ion Battery. ACS Appl. Energy Mater. *4*, 11377–11385.
8. Devulapalli, V.S.D., Kushwaha, R., Ovalle, E., Singh, H.D., Shekhar, P., Chakraborty, D., Vinod, C.P., Vaidhyanathan, R., and Borguet, E. (2022). Synergistic Electronic Effects in AuCo Nanoparticles Stabilized in a Triazine-Based Covalent Organic Framework: A Catalyst for Methyl Orange and Methylene Blue Reduction. ACS Appl. Nano Mater. *5*, 4744–4753.
9. Mi, X., Zhou, S., Zhou, Z., Vakili, M., Qi, Y., Jia, Y., Zhu, D., and Wang, W. (2020). Adsorptive removal of diclofenac sodium from aqueous solution by magnetic COF: Role of hydroxyl group on COF. Colloid Surf. A-Physicochem. Eng. Asp. *603*, 125238.
10. Cui, W.-R., Li, F.-F., Xu, R.-H., Zhang, C.-R., Chen, X.-R., Yan, R.-H., Liang, R.-P., and Qiu, J.-D. (2020). Regenerable Covalent Organic Frameworks for Photo-enhanced Uranium Adsorption from Seawater. Angew. Chem. Int. Ed. *59*, 17684–17690.
11. Cui, W.-R., Zhang, C.-R., Xu, R.-H., Chen, X.-R., Jiang, W., Li, Y.-J., Liang, R.-P., Zhang, L., and Qiu, J.-D. (2021). Rational design of covalent organic frameworks as a groundbreaking uranium capture platform through three synergistic mechanisms. Appl. Catal. B Environ. *294*, 120250.
12. Zhu, L., and Zhang, Y.B. (2017). Crystallization of Covalent Organic Frameworks for Gas Storage Applications. Molecules *22*, 1149.
13. Nandi, S., Collins, S., Chakraborty, D., Banerjee, D., Thallapally, P.K., Woo, T.K., and Vaidhyanathan, R. (2017). Ultralow Parasitic Energy for Postcombustion CO_2 Capture Realized in a Nickel Isonicotinate Metal–Organic Framework with Excellent Moisture Stability. J. Am. Chem. Soc. *139*, 1734–1737.
14. Mullangi, D., Chakraborty, D., Pradeep, A., Koshti, V., Vinod, C.P., Panja, S., Nair, S., and Vaidhyanathan, R. (2018). Highly Stable COF-Supported Co/$Co(OH)_2$ Nanoparticles Heterogeneous Catalyst for Reduction of Nitrile/Nitro Compounds under Mild Conditions. Small *14*, 1801233.
15. Kushwaha, R., Kaleeswaran, D., Haldar, S., Chakraborty, D., Mullangi, D., Borah, A., Vinod, C.P., Murugavel, R., and Vaidhyanathan, R. (2020). Nanoporous Covalent Organic Framework Embedded with Fe/Fe_3O_4 Nanoparticles as Air-Stable Low-Density Nanomagnets. ACS Appl. Nano Mater. *3*, 9088–9096.
16. Haque, N., Biswas, S., Dolai, M., Nandi, D.K., Sarkar, M., and Islam, S.M. (2023). Zinc incorporated covalent organic framework (Zn@DBPG): an efficient catalyst for the synthesis of carbamates through CO_2 and non CO_2 fixation pathways under sustainable condition. Mol. Catal. *536*, 112900.
17. Khatun, R., Biswas, S., Biswas, I.H., Riyajuddin, S., Haque, N., Ghosh, K., and Islam, S.M. (2020). Cu-NPs@COF: A potential heterogeneous catalyst for CO_2 fixation to produce 2-oxazolidinones as well as benzimidazoles under moderate reaction conditions. J. CO_2 Util. *40*, 101180.
18. Sarkar, P., Hazra Chowdhury, A., Biswas, S., Khan, A., and Islam, S.M. (2021). 2D covalent organic framework: a photoactive heterogeneous catalyst for chemical fixation of CO_2 over propargyl amines in water under sunlight. Mater. Today Chem. *21*, 100509.
19. Aijaz, A., and Xu, Q. (2014). Catalysis with Metal Nanoparticles Immobilized within the Pores of Metal-Organic Frameworks. J. Phys. Chem. Lett. *5*, 1400–1411.
20. Wang, Z., Reddy, C.B., Zhou, X., Ibrahim, J.J., and Yang, Y. (2020). Phosphine-Built-in Porous Organic Cage for Stabilization and Boosting the Catalytic Performance of Palladium Nanoparticles in Cross-Coupling of Aryl Halides. ACS Appl. Mater. Interfaces *12*, 53141–53149.
21. Liu, J., Wang, N., and Ma, L. (2020). Recent Advances in Covalent Organic Frameworks for Catalysis. Chem. Asian J. *15*, 338–351.
22. Boily, J.F., and Felmy, A.R. (2008). On the protonation of oxo- and hydroxo-groups of the goethite (alpha-FeOOH) surface: A FTIR spectroscopic investigation of surface O-H stretching vibrations. Geochem. Cosmochim. Acta *72*, 3338–3357.
23. Samata, H., Kimura, D., Saeki, Y., Nagata, Y., and Ozawa, T. (2007). Synthesis of lanthanum oxyhydroxide single crystals using an electrochemical method. J. Cryst. Growth *304*, 448–451.
24. Gracien, B., Ekoko, J., Kanza, K., Lobo, O., Muamba, M., Muswema, J., Senga, J.-F., Mangwala, P., Lobo Omer, M., Mvele Jérémie, L., et al. (2014). Gamma irradiation inducing the synthesis of magnetic Fe_3O_4 nanorod particles in alkaline medium Gamma Irradiation Inducing the Synthesis of Magnetic Fe_3O_4 Nanorod Particles in Alkaline Medium. Int. J. Mater. Sci. Appl. *3*, 339–343.
25. Narayan, R.T. (2015). R., Effect of Crystallinity of β- and β_{bc}-Nickel Hydroxide Samples on Chemical Cycling. Indian J. Mater. Sci.820193
26. Sato, T. (2002). The thermal decomposition of zirconium oxyhydroxide. J. Therm. Anal. Calorim. *69*, 255–265.

27. Kumada, N., Kinomura, N., Kodialam, S., and Sleight, A.W. (1994). Crystal structure of a new lanthanum-bismuth oxyhydroxide: $La_{0.26}Bi_{0.74}OOH$. Mater. Res. Bull. *29*, 497–503.
28. Tarakina, N.V., Tyutyunnik, A.P., Baklanova, Y., Maksimova, L.G., Denisova, T.A., and Neder, R.B. (2013). Crystal structure of a new $HfO(OH)_2$ oxyhydroxide. Powder Diffr. *28*, S510–S518.
29. Devulapalli, V.S.D., Richard, M., Luo, T.-Y., De Souza, M.L., Rosi, N.L., and Borguet, E. (2021). Tuning the Lewis acidity of metal–organic frameworks for enhanced catalysis. Dalton Trans. *50*, 3116–3120.
30. Agrawal, M., Sava Gallis, D.F., Greathouse, J.A., and Sholl, D.S. (2018). How Useful Are Common Simulants of Chemical Warfare Agents at Predicting Adsorption Behavior? J. Phys. Chem. C *122*, 26061–26069.
31. Cavka, J.H., Jakobsen, S., Olsbye, U., Guillou, N., Lamberti, C., Bordiga, S., and Lillerud, K.P. (2008). A new zirconium inorganic building brick forming metal organic frameworks with exceptional stability. J. Am. Chem. Soc. *130*, 13850–13851.
32. Kirlikovali, K.O., Chen, Z., Islamoglu, T., Hupp, J.T., and Farha, O.K. (2020). Zirconium-Based Metal–Organic Frameworks for the Catalytic Hydrolysis of Organophosphorus Nerve Agents. ACS Appl. Mater. Interfaces *12*, 14702–14720.
33. Chen, Z., Wang, X., Noh, H., Ayoub, G., Peterson, G.W., Buru, C.T., Islamoglu, T., and Farha, O.K. (2019). Scalable, room temperature, and water-based synthesis of functionalized zirconium-based metal–organic frameworks for toxic chemical removal. CrystEngComm *21*, 2409–2415.
34. Katz, M.J., Moon, S.-Y., Mondloch, J.E., Beyzavi, M.H., Stephenson, C.J., Hupp, J.T., and Farha, O.K. (2015). Exploiting parameter space in MOFs: a 20-fold enhancement of phosphate-ester hydrolysis with UiO-66-NH_2. Chem. Sci. *6*, 2286–2291.
35. Bůžek, D., Demel, J., and Lang, K. (2018). Zirconium Metal-Organic Framework UiO-66: Stability in an Aqueous Environment and Its Relevance for Organophosphate Degradation. Inorg. Chem. *57*, 14290–14297.
36. Baklanova, Y.V., Denisova, T.A., Maksimova, L.G., Tyutyunnik, A.P., Baklanova, I.V., Shein, I.R., Neder, R.B., and Tarakina, N.V. (2014). Synthesis and characterisation of new $MO(OH)_2$ (M = Zr, Hf) oxyhydroxides and related Li_2MO_3 salts. Dalton Trans. *43*, 2755–2763.
37. Gondal, M.A., Fasasi, T.A., Baig, U., and Mekki, A. (2018). Effects of Oxidizing Media on the Composition, Morphology and Optical Properties of Colloidal Zirconium Oxide Nanoparticles Synthesized via Pulsed Laser Ablation in Liquid Technique. J. Nanosci. Nanotechnol. *18*, 4030–4039.
38. Teeparthi, S.R., Awin, E.W., and Kumar, R. (2018). Dominating role of crystal structure over defect chemistry in black and white zirconia on visible light photocatalytic activity. Sci. Rep. *8*, 5541.
39. Yuan, Y., Wang, J., Adimi, S., Shen, H., Thomas, T., Ma, R., Attfield, J.P., and Yang, M. (2020). Zirconium nitride catalysts surpass platinum for oxygen reduction. Nat. Mater. *19*, 282–286.
40. Appaturi, J.N., Ratti, R., Phoon, B.L., Batagarawa, S.M., Din, I.U., Selvaraj, M., and Ramalingam, R.J. (2021). A review of the recent progress on heterogeneous catalysts for Knoevenagel condensation. Dalton Trans. *50*, 4445–4469.
41. Gogoi, C., Nagarjun, N., Rana, A., Dhakshinamoorthy, A., and Biswas, S. (2022). Diamino group-functionalized Zr-based metal–organic framework for fluorescence sensing of free chlorine in the aqueous phase and Knoevenagel condensation. Dalton Trans. *51*, 6964–6975.
42. Min, H.-K., Cha, S.H., and Hong, S.B. (2013). Nitrided ITQ-2 as an efficient Knoevenagel condensation catalyst. Chem. Commun. *49*, 1115–1117.
43. Dumbre, D.K., Mozammel, T., Selvakannan, P.R., Hamid, S.B.A., Choudhary, V.R., and Bhargava, S.K. (2015). Thermally decomposed mesoporous Nickel Iron hydrotalcite: An active solid-base catalyst for solvent-free Knoevenagel condensation. J. Colloid Interface Sci. *441*, 52–58.
44. Miao, Z., Luan, Y., Qi, C., and Ramella, D. (2016). The synthesis of a bifunctional copper metal organic framework and its application in the aerobic oxidation/Knoevenagel condensation sequential reaction. Dalton Trans. *45*, 13917–13924.
45. Zhang, Y., Wang, C., Zhang, X., Li, H., Li, X., and Lin, Y. (2018). Assembly and Post-modification of Fe_3O_4@MIL-100(Fe) for Knoevenagel Condensation. Chem. Res. Chin. Univ. *62*, 655–662.
46. Wang, D., and Li, Z. (2015). Bi-functional NH2-MIL-101(Fe) for one-pot tandem photo-oxidation/Knoevenagel condensation between aromatic alcohols and active methylene compounds. Catal. Sci. Technol. *5*, 1623–1628.
47. Yang, Q., Zhang, H.-Y., Wang, L., Zhang, Y., and Zhao, J. (2018). Ru/UiO-66 Catalyst for the Reduction of Nitroarenes and Tandem Reaction of Alcohol Oxidation/Knoevenagel Condensation. ACS Omega *3*, 4199–4212.
48. Dhakshinamoorthy, A., Heidenreich, N., Lenzen, D., and Stock, N. (2017). Knoevenagel condensation reaction catalysed by Al-MOFs with CAU-1 and CAU-10-type structures. CrystEngComm *19*, 4187–4193.
49. Feng, L., Wang, K.-Y., Day, G.S., Ryder, M.R., and Zhou, H.-C. (2020). Destruction of Metal–Organic Frameworks: Positive and Negative Aspects of Stability and Lability. Chem. Rev. *120*, 13087–13133.
50. Conley, E.T., and Gates, B.C. (2022). Life History of the Metal–Organic Framework UiO-66 Catalyzing Methanol Dehydration: Synthesis, Activation, Deactivation, and Demise. Chem. Mater. *34*, 3395–3408.
51. Wasson, M.C., Xie, H., Wang, X., Duncan, J.S., and Farha, O.K. (2022). Structural transformation of metal oxo species within UiO-66 type metal–organic frameworks. CrystEngComm *24*, 5135–5140.
52. Vaidhyanathan, R., Mullangi, D., and Nandi, S. (2019). Covalent Organic Frameworks as Porous Supports for Non-noble Metal-Based Water Splitting Electrocatalysts. US Patent, 10301727.
53. Van Beurden, K., de Koning, S., Molendijk, D., and van Schijndel, J. (2020). The Knoevenagel reaction: a review of the unfinished treasure map to forming carbon-carbon bonds. Green Chem. Lett. Rev. *13*, 349–364.
54. Stern, R.D., Kingsbury, R.S., and Persson, K.A. (2021). Aqueous Stability of Zirconium Clusters, Including the Zr(IV) Hexanuclear Hydrolysis Complex $[Zr_6O_4(OH)_4(H_2O)_{24}]^{12+}$, from Density Functional Theory. Inorg. Chem. *60*, 15456–15466.
55. Lubineau, A., Augé, J., and Queneau, Y. (1994). Water-promoted organic reactions. Synthesis *1994*, 741–760.
56. Vijender, M., Kishore, P., and Satyanarayana, B. (2008). Zirconium tetrachloride-SiO_2 catalyzed Knoevenagel condensation: A simple and efficient protocol for the synthesis of substituted electrophilic alkenes. ARKIVOC (Gainesville, FL, U. S.) *2008*, 122–128.
57. Malakooti, R., Mahmoudi, H., Hosseinabadi, R., Petrov, S., and Migliori, A. (2013). Facile synthesis of pure non-monoclinic zirconia nanoparticles and their catalytic activity investigations for Knoevenagel condensation. RSC Adv. *3*, 22353–22359.
58. Liu, F., Kumar, S., Li, S., You, H., Ren, P., and Zhao, L. (2020). Bifunctional design of stable metal-organic framework bearing triazole–carboxylate mixed ligand: Highly efficient heterogeneous catalyst for knoevenagel condensation reaction under mild conditions. Catal. Commun. *142*, 106032.
59. Laha, B., Khullar, S., Gogia, A., and Mandal, S.K. (2020). Effecting structural diversity in a series of Co(II)–organic frameworks by the interplay between rigidity of a dicarboxylate and flexibility of bis(tridentate) spanning ligands. Dalton Trans. *49*, 12298–12310.
60. Zuo, W., Yang, S., Xing, Y., Xiao, X., Fan, D., Li, H., Wang, G., Qin, B., You, S., and Jia, X. (2022). Amorphous zirconium metal–organic frameworks assembled from mixed porphyrins as solvent-free catalysts for Knoevenagel condensation. Dalton Trans. *51*, 6631–6637.
61. Azdad, Z., Marot, L., Moser, L., Steiner, R., and Meyer, E. (2018). Valence band behaviour of zirconium oxide, Photoelectron and Auger spectroscopy study. Sci. Rep. *8*, 16251.
62. Yang, H., Zhang, J., Li, J., Shen, Q., and Zhang, L. (2019). In Situ Preparation and Corrosion Resistance of a ZrO_2 Film on a ZrB_2 Ceramic. Coatings *9*, 455.
63. Al-Doghachi, F.A.J., and Taufiq-Yap, Y.H. (2018). CO_2 Reforming of Methane over Ni/MgO Catalysts Promoted with Zr and La Oxides. ChemistrySelect *3*, 816–827.
64. Mullangi, D., Dhavale, V., Shalini, S., Nandi, S., Collins, S., Woo, T., Kurungot, S., and Vaidhyanathan, R. (2016). R., Low-Overpotential Electrocatalytic Water Splitting with Noble-Metal-Free Nanoparticles Supported in a sp^3 N-Rich Flexible COF. Adv. Energy Mater. *6*, 1600110.
65. Katz, M.J., Mondloch, J.E., Totten, R.K., Park, J.K., Nguyen, S.T., Farha, O.K., and Hupp, J.T. (2014). Simple and Compelling Biomimetic Metal-Organic Framework Catalyst for the Degradation of Nerve Agent Simulants. Angew. Chem. Int. Ed. *53*, 497–501.
66. Su, S., Jung, D., Gong, X., Idrees, K.B., Hanna, S.L., Islamoglu, T., Gianneschi, N.C., and Farha, O.K. (2022). Aggregation-Suppressed Porous Processable Hexa-Zirconium/Polymer Composites for Detoxification of a Nerve Agent Simulant. Chem. Mater. *34*, 4983–4991.

STAR★METHODS

KEY RESOURCES TABLE

REAGENT or RESOURCE	SOURCE	IDENTIFIER
Chemicals, peptides, and recombinant proteins		
All chemicals	Sigma-Aldrich	Can be found from Sigma webpage: https://www.sigmaaldrich.com/IN/en?gclid=CjwKCAjwrranBhAEEiwAzbhNtcdAAWpwRLra4P3fSnz757Q7-RKl7DP3hQcwmyhtsLvE_iTx3rhtmxoC9LAQAvD_BwE
Software and algorithms		
ChemDraw Professional 18.0	PerkinElmer	https://www.perkinelmer.com/category/chemdraw
ImageJ	Schneider et al.[S3]	https://imagej.nih.gov/ij/
Materials Studio	Accelrys	https://www.3ds.com/products-services/biovia/products/molecular-modeling-simulation/biovia-materials-studio/
XPS peak software	Hesse et al.[S4]	https://public.wsu.edu/~scudiero/documents/DownloadingtheXPSPEAK41software.pdf
GrainFind software package	Open access	https://www.math2market.com/geodict-software/geodict-base-modules/analysis/grainfind.html

RESOURCE AVAILABILITY

Lead contact

Further information and requests for resources should be directed to and will be fulfilled by the lead contacts, Ramanathan Vaidhyanathan (vaidhya@acads.iiserpune.ac.in)

Materials availability

This study did not generate new unique reagents. For rest see key resources table in STAR methods.

Data and code availability

- This study did not use or generate any codes.
- The published article includes all datasets generated or analyzed during this study.
- Any additional information required to reanalyze the data reported in this paper are available from the lead contact upon request.

METHOD DETAILS

Methods S1: Synthesis schemes

Synthesis of 2,4,6-triformylresorcinol

2,4,6-Triformylresorcinol was synthesized using a reported procedure.[S1] 65 mmol of resorcinol (7.16 g) was dissolved in 70 mL of trifluoroacetic acid and 20 g of hexamine was added into it. The mixture was refluxed at 120°C for 24 h under N_2 atmosphere. The contents were further heated at 150°C for 3 h and cooled back to 120°C. About 110 mL of 3 N HCl was added to it and heated at 105°C for 30 min. This yielded a dark yellow precipitate, which was filtered off under hot condition. 1H NMR (400 MHz, DMSO-D6): δ = 10.22 (s, 1H), 10.05 (s, 2H), 8.35 (s, 1H) (Figure S34A). ^{13}C NMR (101 MHz, DMSO-D6): δ = 194.42, 190.52, 170.43, 141.22, 116.32, 110.44) (Figure S34B).

A solvothermal reaction was performed on a bulk scale in which phenylenediamine was reacted with triformylresorcinol in mesitylene, dioxane in presence of acetic acid at 120°C for 3 days in a Teflon liner. The product was obtained as brown powder by vacuum filtration and it was washed with an excess of DMF, THF and methanol.

Larger scale synthesis of IISERP-COF15

IISERP-COF15 was synthesized employing our previously reported method with slight modifications.[S2] IISERP-COF15 was synthesized via the solvothermal method on a larger scale in an autoclave. 360 mg (1.8 mmol) of 2,4,6-triformylresorcinol and 300 mg (2.7 mmol) of phenylenediamine were dissolved in a 50 mL mesitylene and 50 mL dioxane solvent mixture. Contents were stirred at room temperature for 4 h. Then 5 mL

of 6 N acetic acid was added and stirred for another 30 min. Then the mixture was frozen in liq. N_2 and kept in the oven for 3 days at 120°C. (Scheme S1) The product was a dark brown precipitate that was washed with methanol. Obtained a yield of 92% with formula $C_{36}N_6O_4H_{24}$ and molecular weight 604.62 $gmol^{-1}$.

Synthesis of $ZrOCl_2$@COF

100 mg of IISERP-COF15 was dispersed in 40 mL of hexane, and the mixture was stirred for about 30 min till the solution became homogeneous. A clear methanolic solution of $ZrOCl_2.8H_2O$ (100 mg in 10 mL of methanol) was added drop by drop to the dispersion over a period of 3 h with vigorous stirring. The contents were stirred for 12 h at room temperature. The loaded COF was filtered from the dispersion after washing with hexane and methanol multiple times to remove any unloaded reactants and dried under vacuum.

Synthesis of $ZrO_x(OH)_y$@COF

100 mg of $ZrOCl_2.8H_2O$ loaded COF was dispersed in 50 mL of double distilled water and was stirred for 30 min 0.1 M NaOH solution was added drop by drop to the above dispersion till the pH became 10–11. The resulting dispersion was stirred for nearly 30 min and filtered by washing with methanol and water multiple times to remove Cl^- ions.

Procedure for Knoevenagel condensation

In a 25 mL round bottom flask containing 0.8 mol % of $ZrO_x(OH)_y$@COF, 1 mmol of malononitrile, 1 mmol of benzaldehyde were added. To this, 5 mL of water was added, and the reaction mixture was kept for stirring at room temperature for a specified time. The progress of the reaction was monitored using TLC. On completion of the reaction, ethyl acetate was added to the reaction mixture, and the catalyst was separated by filtration. The filtered catalyst was washed thoroughly with methanol and water several times, dried, and kept for use in the next cycle of catalysis. The filtrate collected was extracted using ethyl acetate and water, the organic phase was dried with anhydrous Na_2SO_4, and the solvent was evaporated. The crude product obtained was purified using recrystallization or column chromatography and characterized using ^1H and ^{13}C Nuclear Magnetic Resonance Spectroscopy.

Amount of catalyst used in each reaction = 0.8 mol % of $ZrO_x(OH)_y$@COF for 1.0 mmol of reactant, reaction time 0.5 h at 25°C, were added to 5 mL of water.

% of yield = (Actual weight of the yield/predicted weight of the product) x 100;

TON (Turnover number) calculation = moles converted/moles of active sites;

TOF (Turnover frequency) = TON/time in hours.

Procedure for DMNP hydrolysis

In a 3 mL glass vial, 0.8 mol % of $ZrO_x(OH)_y$@COF was added to a 1 mL aqueous solution of 0.45 M N-ethyl morpholine (buffer pH = 10) and stirred for 30 min at ambient temperature. 4 μL (21 μmol) of DMNP was added to the stirred solution. To monitor reaction progress, UV-vis spectra were acquired on a JASCO V630 spectrophotometer (acquisition: 4000 nm/min; interval: 2 nm) at regular time intervals by diluting 20 μL of the reaction mixture in 10 mL of the buffer solution.

GD dose-extraction test

Dose-extraction tests were performed to probe the activity of the sorbent material against soman, GD. ~18 mg of material was measured and placed in an autosampler vial. The samples were dried at 50°C for 2 h, and then humidified overnight at 50% RH and 25°C in a chamber with internal circulation. GD was then dosed to the vial at a ratio of 1.0 μL GD to 10 mg sorbent. After a 24 h incubation period, an extraction was conducted using 1.5 mL acetonitrile and vortexing to create a slurry mixture; the mixture then was filtered and transferred to an autosampler vial, and analysis was performed using a GC equipped with a mass spectrometer. The amount reacted was calculated based on the difference between the amount of GD detected after the incubation period and a blank GD spike of the same quantity.

Instrumentation

Powder X-ray diffraction

Powder XRDs were carried out using a Bruker D8 Advance instrument and Rigaku tabletop instrument. The data analysis was performed using the Reflex module of the Materials Studio V6.

Infrared Spectroscopy

IR spectra were obtained using a Nicolet ID5 attenuated total reflectance IR spectrometer, in the range 4000-600 cm^{-1}, operating at ambient temperature. The solid-state IR spectra were recorded using KBr pellets as background.

Thermogravimetry

NETSZCH TGA-DSC instrument has been used for TGA analysis. The sample was heated under N_2 flow of 20 mL/min (purge + protective) from 25°C to 600°C with a heating rate of 10 K/min.

Field Emission Scanning Electron Microscopy (FESEM)

FESEM images were obtained using an electron microscope equipped with an integral charge compensator and embedded EsB and AsB detectors. An Oxford Xmax instrument 80 mm^2 (Carl Zeiss NTS, Gmbh) was integrated into electron microscope to obtain the EDAX information from the samples. Imaging conditions: 2 kV, WD = 2 mm, magnification: 200 kX, Inlens detector. For SEM images, as an initial preparation, the samples were ground thoroughly, soaked in EtOH for 30 min, and were sonicated for 2 h. These well-dispersed samples were drop cast on silicon wafers and dried under vacuum for at least 12 h.

High-Resolution Transmission Electron Microscopy (HRTEM)

Transmission electron microscopy (TEM) was performed using JEM 2200FS TEM microscope, operating at an accelerating voltage of 200 kV. The diffractograms were recorded at a scanning rate of 1° min^{-1} between 20° and 80°. The images from HRTEM were analyzed using ImageJ software.[S3]

Nuclear Magnetic Resonance spectroscopy (NMR)

NMR spectra for the catalytic products were recorded on a 400 MHz, Jeol, ECS-400, Bruker 400 MHz and solid-state magic angle spinning NMR spectra for COF was obtained in Bruker 500 MHz.

X-ray photoelectron spectroscopy (XPS)

XPS measurements were carried out using Thermo Kalpha+ spectrometer using micro focused and monochromated AlKα radiation with energy 1486.6 eV. The base pressure of the spectrometer was better than 10^{-8} mbar during the spectral acquisition. The pass energy for spectral acquisition was kept at 50 eV for individual core-levels. The electron flood gun was utilized for providing charge compensation during data acquisition. The samples for XPS analysis were prepared inside the glove box and transferred to a vacuum transfer module, which was subsequently evacuated in the anti-chamber of the glove box. The samples were loaded onto the spectrometer using this vacuum transfer module and subsequently pumped down by turbo molecular pumps connected to the load lock chamber. This allowed to efficient transfer of the samples without exopsure to the atmosphere. The peak fitting of the individual core-levels was done using XPS peak software with a Shirley type background.[S4]

Adsorption studies

Adsorption studies were performed using a 3-FLEX pore and surface area analyzer, Micromeritics ASAP. Prior to adsorption, the samples were soaked in Methanol for solvent exchange and evacuation.

UV-Vis Spectroscopy for DMNP hydrolysis

The progress of DMNP hydrolysis was monitored by acquiring UV-vis spectra on a JASCO V630 spectrophotometer (acquisition: 4000 nm/min; interval: 2 nm) at regular time intervals by diluting 20 μL of the reaction mixture in 10 mL of the buffer solution.

3D Tomography

Zr-COF specimens were imaged using X-ray microtomography (Xradia 510 Versa X-ray Microscope, Zeiss X-ray Microscopy, Pleasanton, CA, USA) to study the three-dimensional spatial distribution of Zr inside the COF scaffold. Specimens were loaded onto the sample holder, kept in between the X-ray source and the detector assembly. Detector assembly consisted of a scintillator, 20 X optics and a CCD camera. X-ray source was ramped up to 80 kV and 7 W. The tomographic image acquisitions were completed by acquiring 3201 projections over 360° of rotation with a pixel size of approximately 0.8 microns for a field of view of approximately 0.8 × 0.8 × 0.8 mm^3. Each projection was recorded with 6 s exposure time. In addition, projections without the specimen in the beam (reference images) were also collected and averaged. The filtered back-projection algorithm was used for the reconstruction of the projections to generate two-dimensional (2D) virtual cross-sections of the specimens.

Segmentation and further processing were performed using GeoDict software package (GeoDict 2018, Math2Market GmbH, Germany). 2D images were trimmed down to a sub-volume (approximately 315 × 95 × 450 microns) and filtered to remove noise. During the image segmentation process, the voxels pertaining to Zr particles and COF scaffold in the grayscale histogram were differentiated with the aid of OTSU-mediated threshold selection program. The resultant 3D reconstructed model was used to estimate the particle diameter distribution profile, using GrainFind software package.

Bulk characterizations

Characterizations of IISERP-COF15, ZrOx(OH)y and ZrOx(OH)y@COF

The crystalline nature of the COF was confirmed by Powder X-ray diffraction (Figure S1). The Infra-Red (IR) stretching band at 1609 cm^{-1} is assigned to the vibration of C=O bonds, peaks at 1517 and 1454 cm^{-1} are observed corresponding to the stretching vibrations of C=N and C=C-N bonds, respectively (Figure S2). Thermogravimetric analysis (TGA) shows that IISERP-COF15 has very good thermal stability up to 380°C (Figure S3). COF shows 39% mass loss up to 244°C in two steps which can be attributed to the solvents residing on the COF

surface and solvent molecules occluded in the nanopores. Such large solvent content is typically attributable to microporous structure, and this is consistent with the fact that our COF is built from relatively smaller tripodal monomers. Porosity investigation was done for the as made COF and the permanent porosity was established by N_2 adsorption isotherm at 77 K. It shows a type-I isotherm with a saturation uptake of 16 mmol/g (Figure S4). BET and Langmuir surface areas were estimated using the adsorption branch of nitrogen isotherm and it has come out to be 1369 and 1739 m^2/g, respectively, which is slightly on the higher side than the previously reported by Chakraborty et al. (Figures S5 and S6). NLDFT fit to the adsorption branch of N_2 isotherm shows that COF is microporous and it has a major pore size of 1.3 nm (Figure S7). Microscopic studies were performed to observe the morphology of the COF, FESEM shows that COF has snow grain like morphology, these small grains have aggregated together to give flakes, stacked over each other, like appearance (Figure S8). From HRTEM, lattice planes can be observed which reflect the highly crystalline nature of IISERP-COF15, HRTEM (Figure S15) shows that COF consists of flakes which are overlapped on each other, as observed from FESEM.

Procedures and optimization of catalyzed reactions

ZrOx(OH)y@COF catalysis optimization for Knoevenagel condensation

ZrOx(OH)y@COF acts as a catalyst for C=C formation. The optimal catalyst loading was found to be 0.8 mol %. The catalyst recovered after 10 cycles of reaction was washed thoroughly with water and methanol, dried, and was subjected to various characterization techniques. A wide variety of substrates were studied (Table 1), and all products were characterized at each stage using ^1H, ^{13}C Nuclear Magnetic Resonance Spectroscopy. Control reactions were done by using neat $ZrOCl_2.8H_2O$ and $ZrO_x(OH)_y$ using benzaldehyde as a model substrate at room temperature and water as a solvent resulting in low yields (Table S2). Water was selected as optimal solvent among other solvents (Table S1). Most of the substrates provided an excellent yield of above 90%. Both electron-withdrawing and electron-donating substrates provided good yields with electron-withdrawing substrates giving slightly higher yields.

General procedure for DMNP hydrolysis

A specified amount of catalyst was added to a 1 mL solution of 0.45 M N-ethyl morpholine (buffer pH = 10) and stirred for 30 min at ambient temperature. 4 μL (21 μmol) of "Dimethyl nitrophenyl phosphate (DMNP), a simulant of the nerve agent Soman is added to the stirred solution. DMNP hydrolysis leads to the formation of 4-nitrophenolate and dimethyl hydrogen phosphate as products under basic conditions (pH = 10) (Scheme S3). The dark yellow 4-nitrophenolate has an absorption band that peaks at ~400 nm whose intensity is monitored with time using U.V visible spectroscopy to follow the reaction progress. UV-vis spectra were acquired on a JASCO V630 spectrophotometer (acquisition: 4000 nm/min; interval: 2 nm) at regular intervals by diluting 20 μL of the reaction mixture in 10 mL of the buffer solution.

ZrOx(OH)y@COF as a catalyst for DMNP hydrolysis

It was seen that $ZrO_x(OH_y$@COF catalyzes DMNP hydrolysis. The catalysis was performed using $ZrO_x(OH)_y$@COFand neat $ZrO_x(OH)_y$ and as made COF as control reactions (Table S4). It was seen that $ZrO_x(OH)_y$@COFshows nearly 37% conversion of DMNP in nearly 3 h with abs~ 0.8 (100% DMNP hydrolysis => abs~ 0.8). Individual UV-vis profiles showing the progress of DMNP hydrolysis by $ZrO_x(OH)_y$@COF (Figure S23A), neat $ZrO_x(OH)_y$ (Figure S23B), and as made COF (Figure S23C) are listed below.

Soman degradation

Dose-extraction tests were performed to probe the activity of the sorbent material against soman, GD. ~18 mg of sorbent was measured and placed in an autosampler vial. The samples were dried at 50°C for 2 h, and then humidified overnight at 50% RH and 25°C in a chamber with internal circulation. GD was then dosed to the vial at a ratio of 1.0 μL GD to 10 mg sorbent. After a 24 h incubation period, an extraction was conducted using 1.5 mL acetonitrile and vortexing to create a slurry mixture; the mixture then was filtered and transferred to an autosampler vial, and analysis was performed using a GC equipped with a mass spectrometer. The amount reacted was calculated based on the difference between the amount of GD detected after the incubation period and a blank GD spike of the same quantity.